UCLA
UCLA Previously Published Works

Title

Mechanical Evaluation of Unobstructing Magnetic Microactuators for Implantable Ventricular Catheters

Permalink

https://escholarship.org/uc/item/54v1h5vq

Journal

Journal of Microelectromechanical Systems, 23(4)

ISSN

1057-7157

Authors

Lee, Hyowon
Kolahi, Kameran
Bergsneider, Marvin
et al.

Publication Date

2014-08-01

DOI

10.1109/jmems.2014.2321377

Peer reviewed

Mechanical Evaluation of Unobstructing Magnetic Microactuators for Implantable Ventricular Catheters

Hyowon Lee [Member, IEEE],
NeuroEngineering Training Program, Biomedical Engineering Interdepartmental Program, University of California at Los Angeles, Los Angeles, CA 90095 USA. He is now with the St. Jude Medical, Implantable Electronic Systems Division, Plano, TX 75024 USA (hyowon.lee@ucla.edu)

Kameran Kolahi,
Mathematics Department, University of California at Los Angeles, Los Angeles, CA 90095 USA (kkolahi1@gmail.com)

Marvin Bergsneider, and
NeuroEngineering Training Program, Biomedical Engineering Interdepartmental Program, Neurosurgery, School of Medicine, University of California at Los Angeles, Los Angeles, CA 90095 USA (mbergsneider@mednet.ucla.edu)

Jack W. Judy [Senior Member, IEEE]
NeuroEngineering Training Program, Biomedical Engineering Interdepartmental Program, Department of Electrical Engineering, University of California at Los Angeles, Los Angeles, CA 90095 USA. He is now with the Nanoscience Institute for Medical and Engineering Technology, University of Florida, Gainesville, FL 32611 USA (jack.judy@ieee.org)

Abstract

Here, we report on the development and evaluation of novel unobstructing magnetic microactuators for maintaining the patency of implantable ventricular catheters used in hydrocephalus application. The treatment of hydrocephalus requires chronic implantation of a shunt system to divert excess cerebrospinal fluid from the brain. These shunt systems suffer from a high failure rate (>40%) within the first year of implantation, often due to biological accumulation. Previously, we have shown that magnetic microactuators can be used to remove biological blockage. The new cantilever-based magnetic microactuator presented in this paper improves upon the previous torsional design using a bimorph to induce a postrelease out-of-plane deflection that will prevent the device from occluding the pore at rest. The mechanical evaluations (i.e., postrelease deflection, static and dynamic responses) of fabricated devices are reported and compared with theoretical values.

Index Terms

Magnetic microactuator; implantable MEMS; hydrocephalus; ventricular catheter

I. Introduction

A. Hydrocephalus and Treatment

Hydrocephalus is a severe neurological disorder typically characterized by an abnormal accumulation of cerebrospinal fluid (CSF) in the ventricles of the central nervous system [1]. It is often a congenital issue, however, older patients can also develop hydrocephalus from subarachnoid hemorrhage, head trauma, infection, tumor, or other surgical complication. Neonatal pediatric patients typically demonstrate abnormally large head circumferences because the unfused cranial sutures of newborns allow the head to expand with increased intracranial pressure (ICP) of the underlying ventricular system (Figure 1a). In older children and adults, patients suffer from debilitating problems such as vomiting, nausea, papilledema, blurred or double vision, sunsetting of the eyes, problems with slow growth, balance, poor coordination, gait disturbance, urinary incontinence, lethargy, drowsiness, irritability, memory loss, and changes in personality.

Patients are typically diagnosed with neurological evaluations and via advanced neurological imaging techniques such as ultrasound, computed tomography, magnetic resonance imaging (MRI), and pressure-monitoring devices. Hydrocephalus has surprisingly high rate of occurrence. The National Institute of Health estimates that one in every 500 newborns in the US is diagnosed with hydrocephalus [1]. Unfortunately, there is no cure for hydrocephalus. The treatment of choice for hydrocephalus is the management of ICP using a chronically implanted shunt system. This system of catheters—a valve and tubings—diverts the flow of CSF from the ventricles to other part of the body to be metabolized (Figure 1b).

Malfunctioning shunt systems often result in neurological surgeries to revise or to replace the implanted devices, which are potentially dangerous and costly. Approximately 28,000 shunt-related procedures are performed annually and the associated annual medical cost for treating hydrocephalus exceed $1 billion [2]. Clinical studies have revealed that up to 40% of shunts fail within the first year of implantation [3]–[5] and approximately 85% of patients with shunts undergo more than two shunt-revision surgeries within 10 years of initial implantation [6], [7]. This has catapulted shunt placement and revision surgeries as the most common operations in most neurological centers and as the most common surgeries at the pediatric centers around the country [8].

B. MEMS for Hydrocephalus

Since the 1980's, the field of Micro-Electro-Mechanical Systems (MEMS) has enjoyed a tremendous amount of interest from both academia and industry as the next frontier of technological advancement. There now exist various implantable microscale sensors and transducers for biomedical applications. Recently, several groups have begun to apply MEMS technology to improve hydrocephalus treatment as well.

In 2004, a MEMS CSF shunt system, which includes a wireless pressure sensor, an electromagnetic micropump, and a microcontroller, was proposed and fabricated [9]. Using a phase shift in the impedance of the LC resonant circuit, the change in CSF pressure was measured while the micropump was programmed to function above a certain pressure threshold to drain excess CSF. Other groups have also proposed a similar closed-loop

microscale pressure sensors and micropump systems [10]; however, only proof-of-concept were explored thus far without *in vitro* or *in vivo* evaluations.

More recently, a unique system of microfabricated implantable devices was proposed for the treatment of hydrocephalus. Emam and colleagues have fabricated a microfabricated arachnoid villi (MAV), which comprised of microneedles and microvalve arrays [11]. The microneedles were designed to penetrate into the subarachnoid space and drain excess CSF using a uni-directional Parylene-based microvalve that operate using differential pressure changes. Although MAV is another great example of MEMS-device for hydrocephalus therapy, its potential application may be limited because CSF accumulation in subarachnoid space is usually found in external or *ex vacuo* hydrocephalus, which is not as common as the other types of hydrocephalus (i.e., non-communicating or congenital).

C. Magnetic Microactuators for Ventricular Catheters

Evaluation of explanted devices and clinical studies have suggested that one of the leading causes of shunt failure is due to the obstruction of pores in the ventricular catheter from progressive biological accumulation [8], [12], [13]. Researchers have investigated methods to restore the patency of ventricular catheters using various techniques such as electrocautery [14], laser [15], or ultrasound [16]. However, these recanalization techniques still require invasive surgical intervention to access the occluded catheter. As such, there still exists a great demand for a non-invasive, self-clearing shunt system that requires no additional surgical intervention.

To address this critically unmet need for a ventricular catheter with self-clearing capabilities, we have previously proposed to integrate magnetic microactuators to remove accumulated biological debris. The magnetic microactuators are ideally suited for chronically implanted medical application because they requires no integrated circuits or implanted power supplies, and they can be controlled non-invasively using externally applied magnetic fields [17]. In our previous reports, we have demonstrated torsional magnetic microactuators with large out-of-plane actuation that can remove accumulated inflammatory cells [18]. To alleviate potential concerns of MRI issues of using implantable magnetic microactuators, we have recently reported the mechanical robustness of these devices in severe MRI conditions [19]. The MEMS-fabricated magnetic microactuators were demonstrated to withstand strong static (7 T) and time-varying magnetic field gradients (17 T/m) without mechanical failures.

However, our initial designs of torsional microactuators maintained a horizontal rest position, which occluded much of the catheter pore while in this state (Figure 2 and 3a–b [18]). In this report, we present the fabrication results of novel cantilever-based magnetic microactuators designed to stay clear of the catheter pore while at rest. The overall goal of this effort is to improve the hydrocephalus therapy with the new unobstructing magnetic microactuators by alleviating potential flow-obstruction issue and prolonging the time-to-occlusion for the chronically implanted shunt system.

II. Design

A. Stress-Induced Beam Deflection

The original torsion-beam-based microactuators provided several key advantages: stable movement, well-established mechanical response, and easy cellular coverage for *in vitro* testing. However, the horizontal rest position of torsional device is an undesirable clinical feature as it occludes a large portion of the pore while inactive. The new design needed to have a large post-release out-of-plane deflection to stay clear of the catheter pore at rest. One of the common issues of MEMS-fabrication is the curling or bucking of bimorphs due to intrinsic stress-mismatch. The curling of structures is often undesirable and is ameliorated by relieving intrinsic stresses between layers. However, we sought to use the mechanics of bimorphs to engineer a specific post-release deflection by controlling the thicknesses and the amount of stresses in the bimorph layers. With this simple approach, we redesigned the magnetic microactuators to have a cantilever-based actuation to achieve a specific post-release deflection (Figure 4).

A layer of plasma-enhanced chemical vapor deposition (PECVD) silicon nitride was chosen as the stress-inducing film for its high-intrinsic stress (~1 GPa) and for its physical robustness. The thickness of the stress-inducing layer was calculated using the well-established Stoney's equation [20]

$$K = \frac{6 t_f \sigma_f}{E_s t_s^2} \quad (1)$$

with the curvature of the composite K, the film stress σ_f, the biaxial modulus of the substrate E_s, and the film and substrate thicknesses t_s and t_f.

A well described limitation of the approximation using Stoney's equation is that the thickness ratio δ between the coating and the substrate needs to be approximately 10% or less [21]. In cases where $\delta > 0.1$, the following equation may be used to describe the curvature of a bilayer [21], [22]

$$K = \frac{-E_s t_s E_f t_f (t_s + t_f)}{G (E_s t_s + E_f t_f)} \Delta \varepsilon, \quad (2)$$

where

$$G = E_s t_s^2 \left(\frac{t_f}{2} - \frac{t_s}{6} - \pi \right) - E_f t_f \left[t_s \left(t_s + \frac{t_f}{2} \right) + \frac{t_f^2}{6} + \pi (2 t_s + t_f) \right], \quad (3)$$

with the biaxial modulus of the film E_f, the thickness of the film t_f, and the strain differential ε. The correction factor for the neutral axis π can be expressed as

$$\pi = \frac{t_s t_f (E_s - E_f)}{2(E_s t_s + E_f t_f)}.$$ (4)

The elastic moduli for the low-pressure chemical vapor deposition (LPCVD) and the PECVD silicon nitride that form the bimorph were obtained from the literature [23]–[25]. The parameters used for the bimorph-bending simulations are listed in Table I. Figure 5 illustrates the relationship between angular deflection and the silicon-nitride thickness for a 600-μm-long, 1-μm-thick cantilever beam made of LPCVD silicon nitride. An angular deflection of approximately −60° was chosen as the target value. As such, the fabrication process included the deposition and the patterning of a 100-nm-thick PECVD layer (Figure 5).

The beam-bending due to the stress-mismatch was also simulated using a 3D COMSOL Multiphysics (V3.5, COMSOL, Inc., Burlington, MA, USA) structural-mechanics model. The cross-section plot of the deflection along the beam length was used to approximate the curvature and the maximum angular deflection (−57.5°), which corresponded closely with the analytical approximation.

III. Fabrication Process

Figure 6 illustrates the top and cross-sectional views of the fabrication process for cantilever-based unobstructing magnetic microactuators. A detailed description of the fabrication process for the torsional magnetic microactuators has previously been documented [18]. The fabrication process for the new cantilever-based microactuator design incorporated additional steps to deposit and pattern the stress-inducing top nitride layer [26]. The actuation sequence of a fabricated device with the maximum magnet volume can be seen in Figure 7.

IV. Characterization Methods

The vertical deflection z of the released microactuators was measured using an optical microscope. Similarly, the static responses of the magnetic microactuators were recorded in the optical microscope using an increasing magnetic field strength. The ac and dc magnetic field strength from the electromagnet was verified by measuring the field using a gaussmeter (6010 FW Bell, Sypris Test and Measurement, Louisville, KY, USA).

The dc response of magnetic field from the electromagnet and its magnetic field were linear (H = 10300±20 A/m/A) and its frequency response was flat until rolling off at up to 2 kHz ($f_{low–pass}$ (3 *dB*) = 2.42 kHz). With the electromagnet, the resonant frequencies of the microactuators were characterized using a dual-beam laser Doppler vibrometer system (Polytec Inc. OFV-552, OFV-5000, Irvine, CA, USA) and a custom LabVIEW signal generation/acquisition software (LabVIEW 2008, National Instruments, Austin TX, USA,).

V. Results

A. Post-Release Deflection

The intrinsic stress of the PECVD silicon-nitride layer was measured to be −992 MPa (Tencor FLX-2320, Milpitas, California, USA). To facilitate comparison, the resulting curvature due to strain-mismatch was converted into a downward vertical displacement z. The vertical deflection can then be converted into angular deflection ϕ using the simple trigonometric relationship between the radius of curvature of the bilayer beam R and the angular deflection ϕ. The radius of curvature R can be defined by

$$R = \frac{1}{K} = \frac{l}{\phi}, \quad (5)$$

with the bilayer beam length l. The deflection magnitude along the z-axis of the bilayer then can be expressed as

$$z_{bl} = 2R \sin^2\left(\frac{\phi}{2}\right). \quad (6)$$

According to theory (Eqs 1, 2), the width of the bilayer has no effect on the resulting curvature. However, as can be seen in Figure 8, the post-release deflection magnitude of 500-μm-diameter actuators with cantilevers of equal lengths varied with beam width. This is likely due to the fact that the volume, and hence mass, of the magnetic plate was not the same for all devices. Instead, devices with shorter beams had more massive structural plates and magnetic elements.

The additional deflection on a curved beam due to the gravitational force on the magnetic microactuator mass z_{mass} can be described as follows [27]:

$$z_{mass} = \frac{\phi m_t gR}{2E_c A} + \frac{3\phi m_t gR}{AG} + \frac{m_t gR^3}{2E_c I}, \quad (7)$$

with the mass of the structural layer and the magnet m_t, the gravitational acceleration g, the elastic modulus of the composite beam E_c, the cross sectional area of the beam A, the shear modulus G, and the moment of inertia I. The total deflection is then the sum of z_{bl} and z_{mass}. Figure 8 illustrates the total deflection as a function of various cantilever-beam widths for several beam lengths. Table II lists the percent difference between the measured and theoretical post-release deflection.

B. Static Response

The vertical deflections of the magnetic microactuators in response to applied static magnetic field were measured using the aforementioned microscope-based optical setup. The measured z-axis position was converted into deflection angle using Eqs. 5–6 (Figure 9).

The theoretical mechanics of flexure-based magnetic microactuator are well documented in literature [28]. In the presence of a magnetic field, the ferromagnetic element generates torque at the end of the bilayer cantilever and causes the device to deflect out of the plane. The deflection angle of the cantilever can be described by the following equation:

$$\phi = \frac{\nu \cdot (\vec{M} \times \vec{H})}{k_\phi}, \quad (8)$$

with angular rotation ϕ, magnet volume ν, induced magnetization vector $\vec{M}$, applied magnetic field vector $\vec{H}$, and the angular cantilever stiffness k_ϕ. The angular stiffness of the cantilever beam is defined by [29]

$$k_\phi = \frac{E_c \mathrm{w} \mathrm{t}^3}{12l}. \quad (9)$$

A plot of the measured and theoretical angular deflection of a cantilever design is shown in Figure 10.

C. Dynamic Response

a) Rayleigh-ritz approximation—The dynamic response of a system with distributed mass, such as the one found in this work, can be estimated using the well-known Rayleigh-Ritz approximation [30]. This method uses the general principle of energy conservation, where the total energy remains constant in the system. Thus, the maximum kinetic energy W_k and the maximum potential energy W_e are equal.

The kinetic energy of a system is

$$W_k = \frac{1}{2} \rho m \upsilon^2. \quad (10)$$

with the density ρ, the mass m, and the velocity υ. The velocity of our actuator can be found using a quasi-static beam displacement function $w(x)$, which provides vertical displacement w as function of position along the beam x. The time dependent displacement function $w(x, t)$ can be written as

$$w(x, t) = w(x)\cos(\omega t), \quad (11)$$

with the time t. The maximum magnitude of velocity υ_{max}, which occurs when $\omega t = \pi/2$ is then

$$v_{\max}(x) = \frac{\partial \hat{w}(x,t)}{\partial t}\bigg|_{\omega t = \pi/2} = -\omega \cdot w(x). \tag{12}$$

Using $v_{\max}$, we can find the maximum kinetic energy for a unit length of the cantilever $\hat{W}_k$

$$\hat{W}_k = \frac{1}{2}\rho(x)v_{\max}(x)^2. \tag{13}$$

We can then obtain the total kinetic energy by integrating $\hat{W}_k$ over the volume of the beam

$$W_k = \frac{\omega^2}{2}\int_V \rho(x)w(x)^2 \mathrm{dV}. \tag{14}$$

For our cantilever-based magnetic microactuator beam, the quasistatic displacement function $w(x)$ is [29]

$$w(x) = \frac{F}{6\mathrm{EI}}(3l_b x^2 - x^3), \tag{15}$$

with the applied force F, the beam length l_b, the beam elastic modulus E, and the beam moment of inertia I. The device contains three separate mass components that contribute to the total kinetic energy: the beam, the structural plate, and the magnet. The kinetic energy from the beam is

$$W_{k,\mathrm{beam}} = \frac{11\omega^2}{840}\rho_b w_b t_b l_b{}^7\left(\frac{F}{\mathrm{EI}}\right)^2, \tag{16}$$

with the density ρ_b, the width w_b, and the thickness t_b of the beam. The kinetic energy from the structural plate is

$$W_{k,\mathrm{sp}} = \frac{\omega^2}{18}\rho_{\mathrm{sp}}v_{\mathrm{sp}}l_b{}^6\left(\frac{F}{\mathrm{EI}}\right)^2, \tag{17}$$

with the density ρ_{sp} and the volume v_{sp} of the structural plate. The kinetic energy from the magnetic element is

$$W_{k,\mathrm{mag}} = \frac{\omega^2}{18}\rho_{\mathrm{mag}}v_{\mathrm{mag}}l_b{}^6\left(\frac{F}{\mathrm{EI}}\right)^2, \tag{18}$$

with the density ρ_{mag} and the volume v_{mag} of the structural plate. The total kinetic energy is then

$$W_{k,tot} = W_{k,beam} + W_{k,sp} + W_{k,mag} = \frac{\omega^2 l_b{}^6}{2520}(33m_b + 140m_{sp} + 140m_{mag})\left(\frac{F}{EI}\right)^2, \quad (19)$$

with the mass of the beam m_b, the structural plate m_{sp}, and the magnet m_{mag}. The potential energy stored in the beam caused by the bending strain is

$$W_p = \int_0^{l_b} \frac{M(x)^2}{2EI} dx, \quad (20)$$

with the moment $M(x) = F(l_b - x)$. Integrating over the length of the beam, the total potential energy is then

$$W_p = \frac{F^2 l_b{}^3}{6EI}. \quad (21)$$

Finally, the primary resonant frequency of the system ω can be found by equating the maximum kinetic energy (Eq. 19) to the maximum potential energy (Eq. 21)

$$\omega^2 = \frac{420EI}{l_b{}^3(33m_b + 140m_{sp} + 140m_{mag})}. \quad (22)$$

A Matlab (Mathworks, Natick, MA) program was used to facilitate evaluation of the primary resonant frequency for devices with various geometries. Using the parameters listed on Table III, the resonant frequency of a sample device was calculated to be approximately 53.7 Hz.

b) Numerical analysis—The dynamic response of cantilever-based magnetic microactuators can also be simulated using a 3D COMSOL Multiphysics MEMS module (v3.5 COMSOL, Inc., Los Angeles, CA, USA). The frequency response analysis used the parameters shown on Table III, sweeping from 1 Hz to 1 kHz in frequency in 1-Hz increments. The resulting dynamic response for a sample device was used to confirm the analytical methods discussed previously and the experimental results. The primary resonant frequency of the sample device was found to be 52.9 Hz, which is in good agreement with the value approximated by the Rayleigh-Ritz methods.

c) Experimental results—The dynamic response of a cantilever-based magnetic microactuator device and its corresponding FEM simulated plots are shown in Figure 11. Although the relative amplitude of each resonant peak is different, the resonant frequencies correspond well with the predicted values. Table IV lists the resonant frequency values for

the sample device shown in Figure 11 compared to the theoretical values predicted by two different methods. The value estimated by the Rayleigh-Ritz method is approximately 5.3% greater than measured. Since the quasi-static displacement function is only an approximation of the real eigenfunction, the result is typically higher than the actual resonant frequency [30], [31]. However, the Rayleigh-Ritz method allows for faster estimation of the primary resonant frequency compared to COMSOL. Thus, we used this approximation to compare the resonant frequencies of various designs of magnetic microactuators with varying beam lengths and widths. Figure 12 illustrates the difference between measured versus theoretical values for devices with various beam geometry. As seen from the sample device, the measured primary resonant frequency corresponded well with the predicted value.

VI. Conclusions

Here we have reported on the fabrication results of cantilever-based unobstructing magnetic microactuators to be used for chronically implanted catheters. The ultimate goal of this research is to integrate MEMS-fabricated microdevices into ventricular catheters to improve hydrocephalus therapy by alleviating issues of CSF flow obstruction and by reducing the number of costly revision surgeries for hydrocephalus patients. The results indicate good control of beam deflection using a bimorph to ensure that the cantilever-based magnetic microactuator does not obstruct the catheter pore at its rest position compared to the torsional design (73% vs. 16%). Moreover, the static and dynamic responses of fabricated devices corresponded well with theory, suggesting good control of fabrication and device mechanics.

A major concern for the development of implantable magnetic microactuators is the potentially adverse impact of strong magnetic fields present in MRI systems. Previously, the torsional magnetic microactuators have been demonstrated to be robust enough to withstand up to 7 T MRI scanner [19]. Although cantilever-based microactuators do have greater ranges of motion than the torsional models, the resulting device movements are physically constrained by surrounding bulk and may easily be accommodated for mechanically, even in arbitrary strong uniform magnetic fields. For example, the cantilever beam described in Table III will experience 1.44 GPa of stress even when bent into a complete circle. Even if the device twists about the long axis of the cantilever due to shape anisotropy, the maximum rotation will be limited to <90° in a stationary patient, which results in a shear stress of 275 MPa for the same beam geometry [29]. These extreme static stress values are well below the 6-GPa fracture strength of LPCVD silicon nitride [24].

The cantilever beam may also experience a compound motion due to changing magnetic-field direction or due to patient movements within the MR environment. Although quantifying the impact of complex static motions is not as straightforward, there are several design solutions that may alleviate potential robustness concerns. For example, a round soft ferromagnetic element may allow the magnetization direction to rotate readily regardless of the applied magnetic field direction to limit lateral and twisting actuation. Moreover, features such as fillets, multiple-beams, or wider-beams may reinforce structural integrity and prevent undesirable movements due to magnetic field orientation and patient movements. Nevertheless, additional experimental evaluations such as those performed for

the torsional design [19] will also be necessary for cantilever-based magnetic microactuators to quantify potential MRI-interactions (i.e., mechanical robustness, RF-heating, and image artifacts).

Ultimately, the clinical efficacy of our MEMS devices in improving hydrocephalus therapy depends on their obstruction-removal capabilities. We are encouraged with our prior work that has demonstrated cell-removal capabilities of torsional magnetic microactuators in a static cell-culture environment [18]. With a greater range of actuation, we expect to see an improvement in cell-removal capabilities with cantilever-based magnetic microactuators. However, additional evaluations must taken into account the fact that implanted devices will be subjected to a continuous CSF flow through its pores. Therefore, our future plan includes *in vitro* evaluations in a circulating biofouling environment to demonstrate the cell-clearing capabilities of these new microdevices against inflammatory cells found in human CSF, which are thought to be responsible for obstructing the ventricular catheters.

Acknowledgments

References

1. National Institute of Neurological Disorders and Stroke NINDS Hydrocephalus Information Page. 2009 Sep. [Online]. Available: http://www.ninds.nih.gov/health_and_medical/disorders/hydrocephalus.htm

2. Patwardhan RV, Nanda A. Implanted ventricular shunts in the United States: The billion-dollar-a-year cost of hydrocephalus treatment. Neurosurgery. 2005; 56(1):139–145. [PubMed: 15617596]

3. Pollack I, Albright A, Adelson P. A randomized, controlled study of a programmable shunt valve versus a conventional valve for patients with hydrocephalus. Neurosurgery. 1999; 45(6):1399–1411. [PubMed: 10598708]

4. Kestle J, et al. Long-term follow-up date from the shunt design trial. Pediatric Neurosurgery. 2000; 33(5):230–236. [PubMed: 11155058]

5. McGirt MJ, et al. Cerebrospinal fluid shunt survival and etiology of failures: A seven-year institutional experience. Pediatric Neurosurgery. 2002; 36(5):248–255. [PubMed: 12053043]

6. Sainte-Rose C, et al. Mechanical complications in shunts. Pediatric Neurosurgery. 1991; 17(1):2–9. [PubMed: 1811706]

7. Choux, M.Di Rocco, C.Hockley, AD., Walker, ML., editors. Pediatric Neurosurgery. London, UK: Churchill Livingstone; 1999.

8. Drake, JM., Sainte-Rose, C., editors. The Shunt Book. Hoboken, NJ, USA: Wiley-Blackwell; 1995.

9. Yoon HJ, Jung JM, Jeong JS, Yang SS. Microdevices for a cerebrospinal fluid (CSF) shunt system. Sens. Actuators A, Phys. 2004; 110(1):68–76.

10. Morganti, E., Pignatel, GU. Proc. 1st Int. Conf. Sens. Technol. Palmerston North; New Zealand: Nov. 2005 Microfluidics for the treatment of the hydrocephalus; p. 483-487.

11. Emam M, et al. A novel microdevice for the treatment of hydrocephalus: Design and fabrication of an array of microvalves and microneedles. Microsyst. Technol. 2008; 14(3):371–378.

12. Gower DJ, Lewis JC, Kelly DL. Sterile shunt malfunction—A scanning electron microscope perspective. J Neurosurgery. 1984; 61(6):1079–1084.

13. Lazareff JA, Peacock W, Holly L, Ver Halen J, Wong A, Olmstead A. Multiple shunt failures: An analysis of relevant factors. Child's Nervous Syst. 1998; 14(6):271–275.

14. Pattisapu JV, Trumble ER, Taylor KR, Howard PD, Kovach TM. Percutaneous endoscopic recanalization of the catheter. Eur. J. Pediatric Surgery. 2000; 45(6):46–47.

15. Chrstens-Barry WA, Guarnieri M, Carson BS Sr. Fiberoptic delivery of laser energy to remove occlusions from ventricular shunts: Technical report. Neurosurgery. 1999; 44(2):345–350. [PubMed: 9932888]

16. Ginsberg HJ, Drake JM, Peterson TM, Cobbold R. Recanalization of obstructed cerebrospinal fluid ventricular catheters using ultrasonic cavitation. Neurosurgery. 2006; 59(4):403–412.

17. Judy JW, Muller RS. Magnetic microactuation of torsional polysilicon structures. Sens. Actuators A, Phys. 1996; 53(1):392–396.

18. Lee SA, Lee H, Pinney JR, Khialeeva E, Bergsneider M, Judy JW. Development of microfabricated magnetic actuators for cellular occlusion removal. J Micromech. Microeng. 2011; 21(5):054006.

19. Lee H, Xu Q, Shellock F, Bergsneider M, Judy JW. Evaluation of magnetic resonance imaging issues for implantable microfabricated magnetic actuators. Biomed. Microdevices. 2014; 16(1):153–161. [PubMed: 24077662]

20. Stoney GG. The tension of metallic films deposited by electrolysis. Proc. Roy. Soc. London A. 1909; 82(553):172–175.

21. Klein CA. How accurate are Stoney's equation and recent modifications. J Appl. Phys. 2000; 88(9):5487–5489.

22. Townsend PH, Barnett DM, Brunner TA. Elastic relationships in layered composite media with approximation for the case of thin films on a thick substrate. J Appl. Phys. 1987; 62(11):4438–4444.

23. Stoffel A, Kóvacs A, Kronast W, Müller B. LPCVD against PECVD for micromechanical applications. J Micromech. Microeng. 1996; 6(1):1–13.

24. Chuang WH, Luger T, Fettig R, Ghodssi R. Characterization of mechanical properties of silicon nitride thin films for space applications. Mater. Res. Soc. Symp. Proc. 2004; 782:A5.21.1-1–A5.21.1-6.

25. Walmsley BA, Liu Y, Hu LX, Bush MB, Dell JM, Faraone LF. Poisson's ratio of low-temperature PECVD silicon nitride thin films. J Microelectromech. Syst. 2007; 16(3):622–627.

26. Lee, H., Lee, S., Bergsneider, M., Judy, JW. Proc. 15th Int. Conf. Solid-State Sens., Actuators, Microsyst. Denver, CO, USA: Jun. 2009 Unobstructing magnetic microactuators for implantable catheters.

27. Shigley, JE. Mechanical Engineering Design. New York, NY, USA: McGraw-Hill; 1983.

28. Judy JW, Muller RS, Zappe HH. Magnetic microactuation of polysilicon flexure structures. J Microelectromech. Syst. 1995; 4(4):162–169.

29. Roark, RJ. Roark's Formulas for Stress and Strain. New York, NY, USA: McGraw-Hill; 1989.

30. Bao, M-H. Micro Mechanical Transducers: Pressure Sensors, Accelerometers, and Gyroscopes. Amsterdam, The Netherlands: Elsevier; 2000.

31. Weaver, W., Timoshenko, SP., Young, DH. Vibration Problems in Engineering. Hoboken, NJ, USA: Wiley; 1990.

Biographies

Hyowon Lee received a B.A. degree in Neuroscience from the Colorado College, in 2004, and an M.S and a Ph.D. in Biomedical Engineering from the University of California, Los

Angeles, in 2008 and 2011, respectively. His research interest include neuroengineering, neurophysiology, implantable medical devices, MEMS-cell interface, and magnetic MEMS. He is a recipient of the NSF IGERT NeuroEngineering Training Fellowship in 2005 and the NIH Ruth L. Kirschstein NRSA Fellowship in 2008.

Kameran Kolahi received a B.S. degree in Mathematics in 2014 from the University of California, Los Angeles and is working towards a Ph.D. in Mathematics from the University of California, Irvine.

Marvin Bergsneider received a B.S. in Electrical Engineering in 1983 from the University of Arizona, followed by a M.D. degree in 1987 from the University of Arizona College of Medicine. He obtained his neurosurgical residency training at UCLA, where he joined the faculty in 1994. He is a Professor of Neurosurgery and a faculty member of the UCLA Biomedical Engineering Interdepartmental Program. His research interests include modeling of intracranial fluid biomechanics and hydrocephalus, plus bioMEMS development.

Jack W. Judy received the Ph.D. and M.S. degrees from the University of California, Berkeley, CA, in 1996 and 1994 respectively, as well as the B.S.E.E. degree, with summa cum laude honors, from the University of Minnesota, Minneapolis, MN, in 1989. He was with the faculty of the Electrical Engineering Department at the University of California, Los Angeles, from 1997 to 2013. From 2009 to 2013, he worked as a program manger in the Microsystems Technology Office (MTO) of the Defense Advanced Research Projects Agency (DARPA). At DARPA he initiated and managed the Reliable Neural Interface

Technology (RENET) Program. He is now with the Nanoscience Institute for Medical and Engineering Technology at the University of Florid, Gainesville. His present research interests include additional novel ferromagnetic MEMS and NEMS devices, chemical sensors, micromachined instruments for plasma research, and a variety of advanced neuroengineering projects, such as advanced neurosurgical microdevices, reliable high-density bi-directional neural-interface systems, and miniaturized high-resolution neural-imaging technologies.
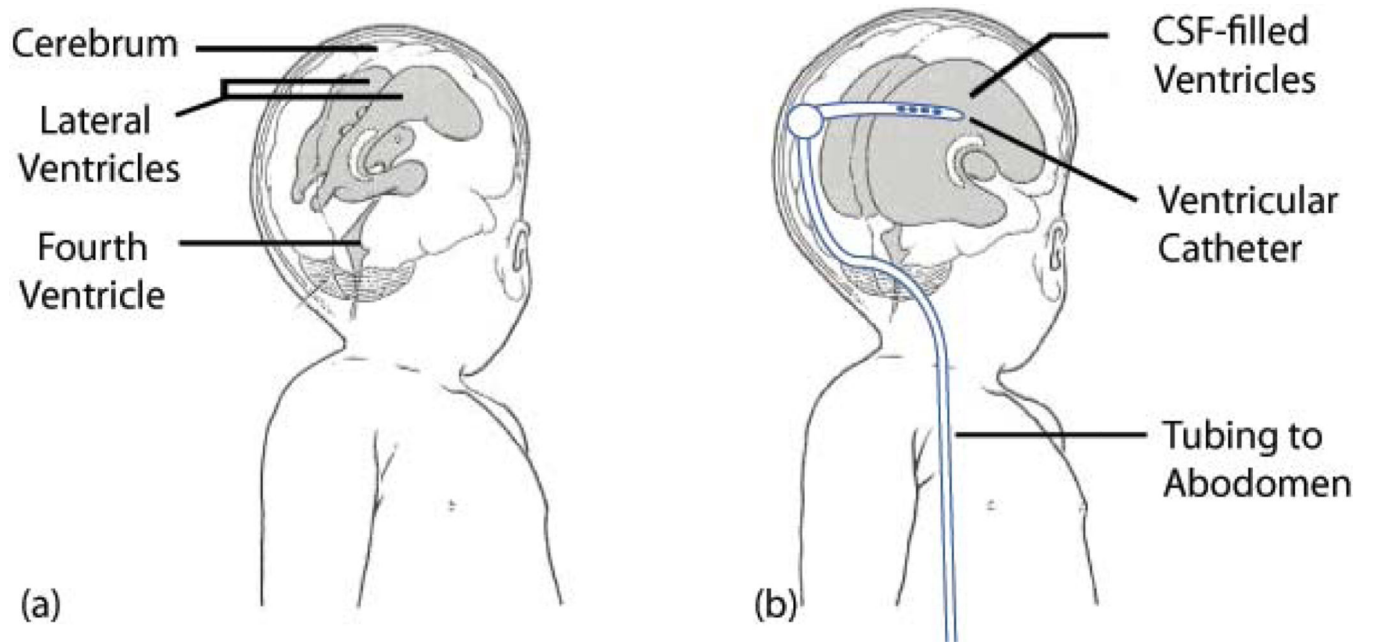
Fig. 1.
Illustration of pediatric hydrocephalus patient: (a) an infant with a normal sized ventricular system, (b) an infant with hydrocephalus. Note the CSF-filled ventricles have expanded the cranial space and are exerting pressure to the surrounding cerebrum.
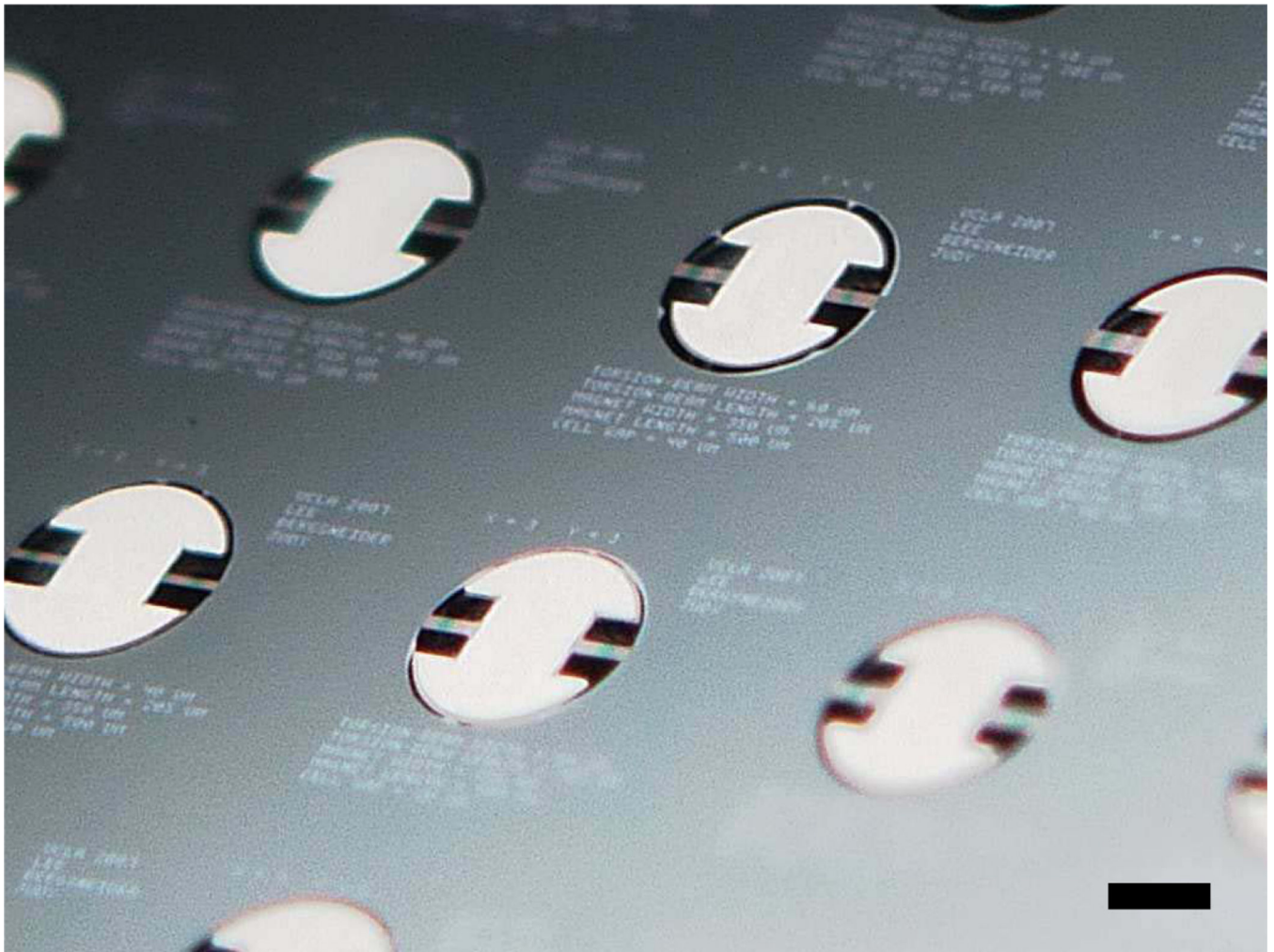
Fig. 2.
Torsional microactuators upon release. Note that when the device is in its flat rest position, it occupies a large fraction of the flow-pore area (~ 73%). Scalebar = 400 μm.
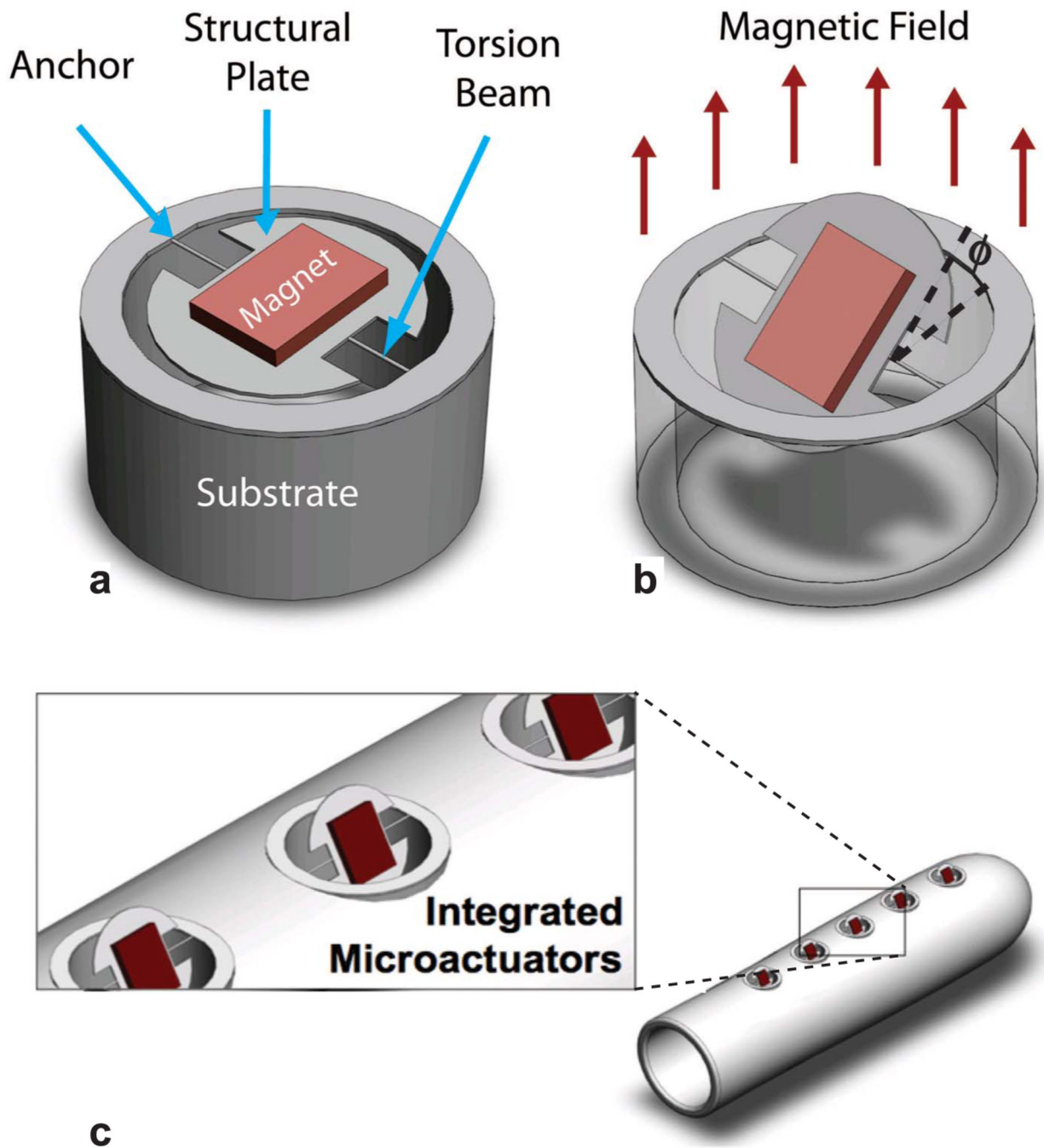
Fig. 3.
A set of 3D schematic diagrams of the torsional magnetic microactuators: (a) unactuated released state, (b) actuated device with an applied magnetic field, (c) a schematic of the proposed MEMS-enabled ventricular catheter.
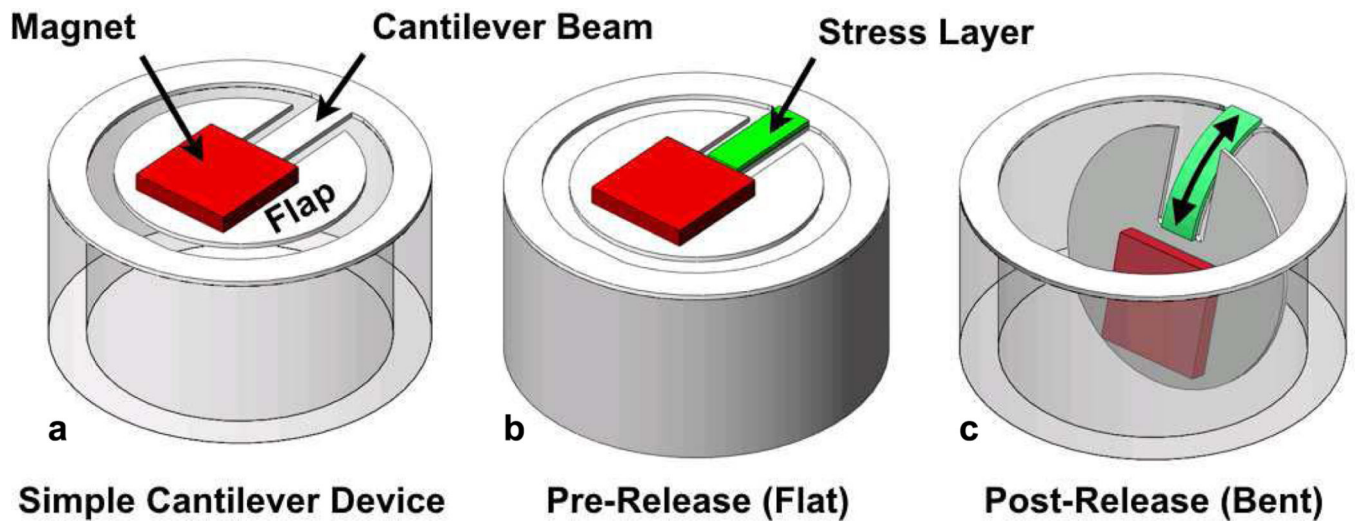
Fig. 4.
Illustrations of flow pores containing a cantilever-based magnetic microactuator: (a) released cantilever device in its rest state without stressinducing layer, (b) unreleased cantilever with devices with compressively stressed layer patterned on the beam, (c) released device from (b) in its rest state.
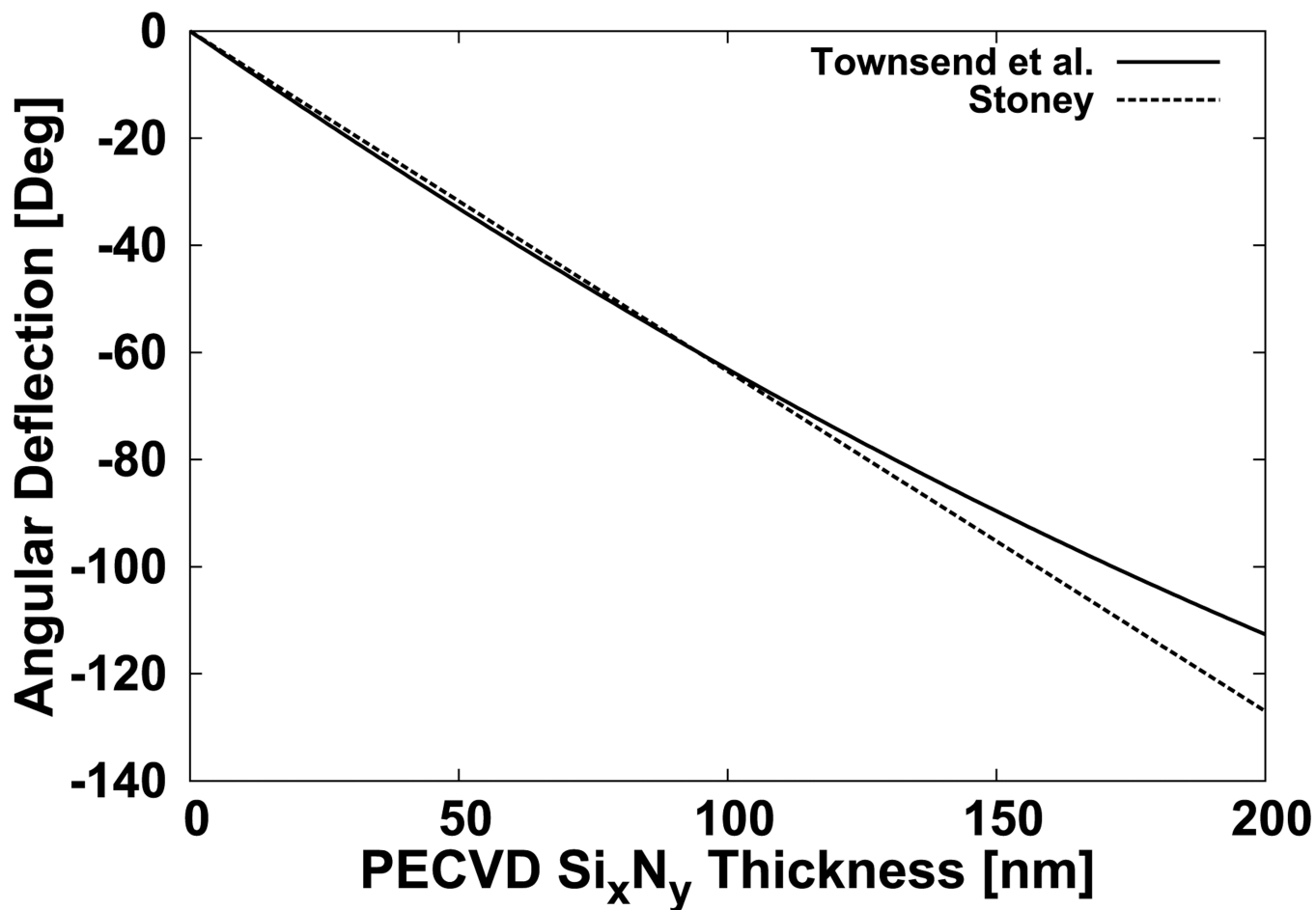
Fig. 5.
The angular deflection of a 600-μm-long, 1-μm-thick LPCVD silicon nitride beam as a function of thickness of a PECVD silicon nitride layer deposited on top. Note that approximately −60° can be achieved with a PECVD silicon nitride layer of 100 nm.
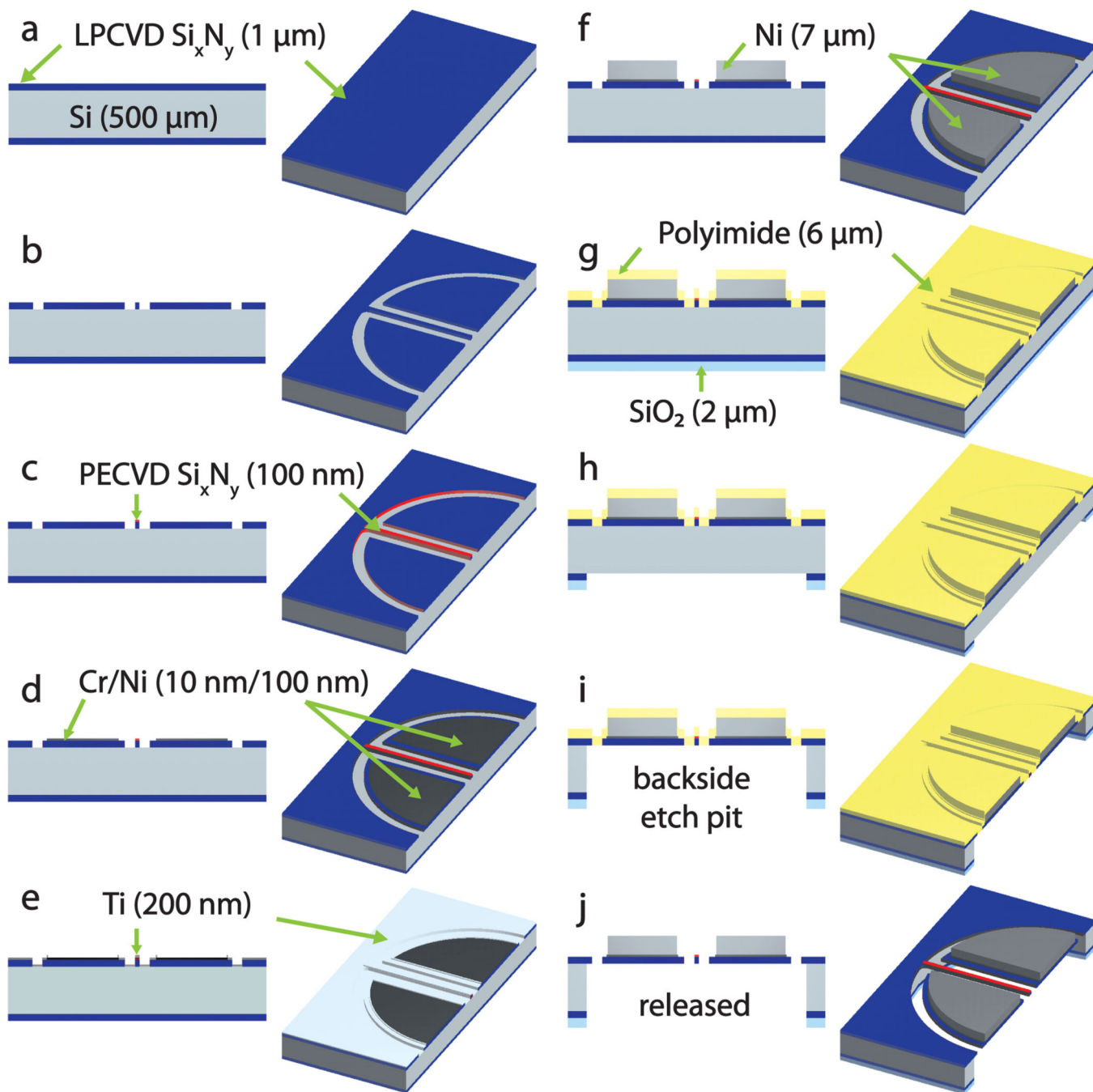
Fig. 6.
Fabrication process for the round single-cantilever microactuator. Refer to Figure 4 for illustration of a fully-released device. Si: single crystal silicon; Si_xN_y: silicon nitride; Cr: chromium; Ni: nickel; Ti: titanium; SiO_2: silicon dioxide. See [26] for detailed description of the fabrication process.
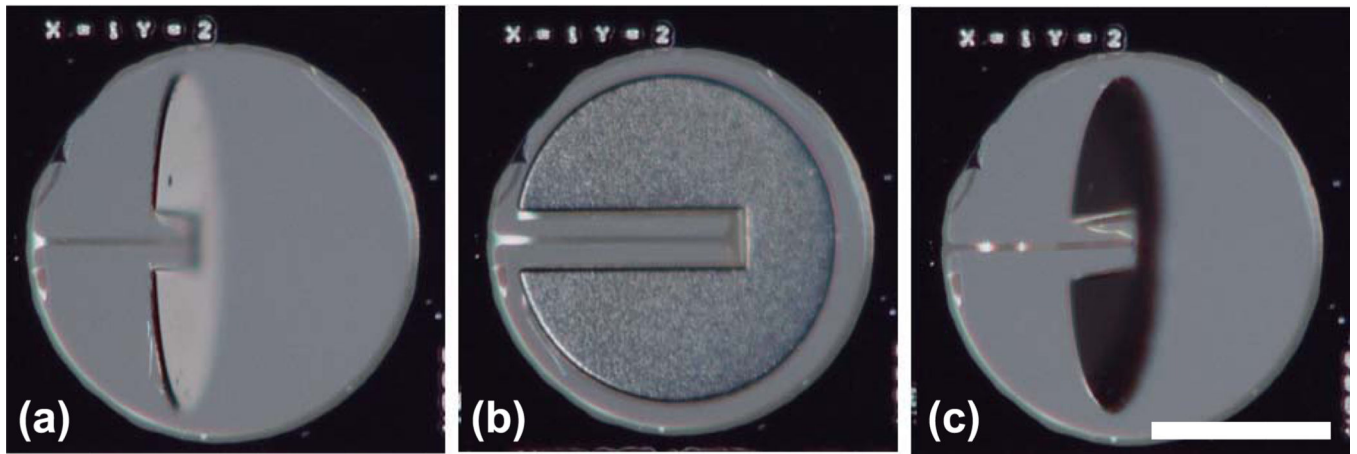
Fig. 7.
Sequential movement of a round single-cantilever magnetic microactuator: (a) device at rest (deflected downwards), (b) device actuated to a flat position (H = 6 kA/m), (c) device actuated up above the flow pore (H = 15 kA/m). Note that the device occupies ~16% of pore surface at rest. Scalebar = 500 μm.
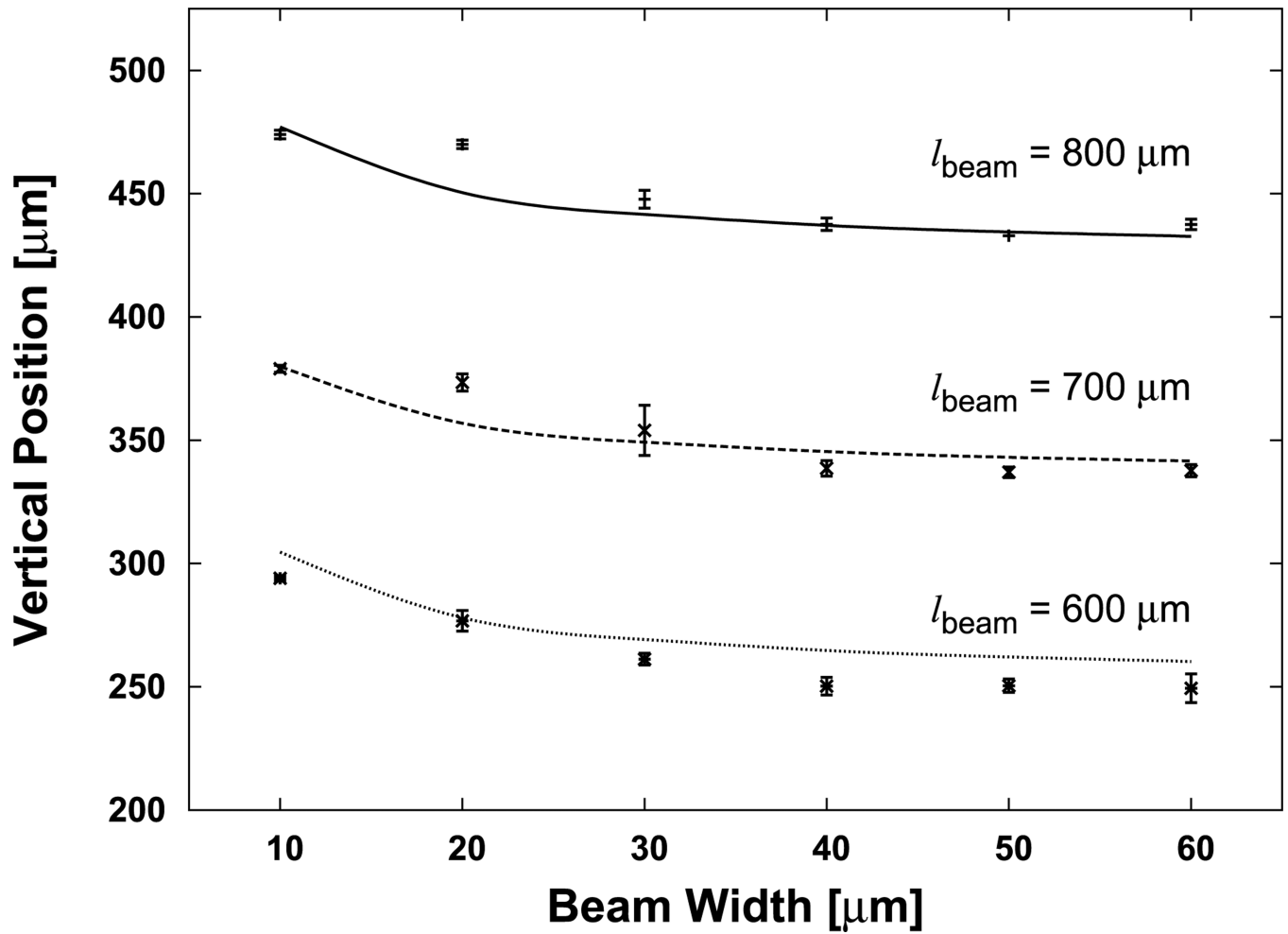
Fig. 8.
Plot of the post-release beam deflection amount for three different beam lengths as a function of beam width. The lines indicate expected values. The results are expressed as average ± s. d.
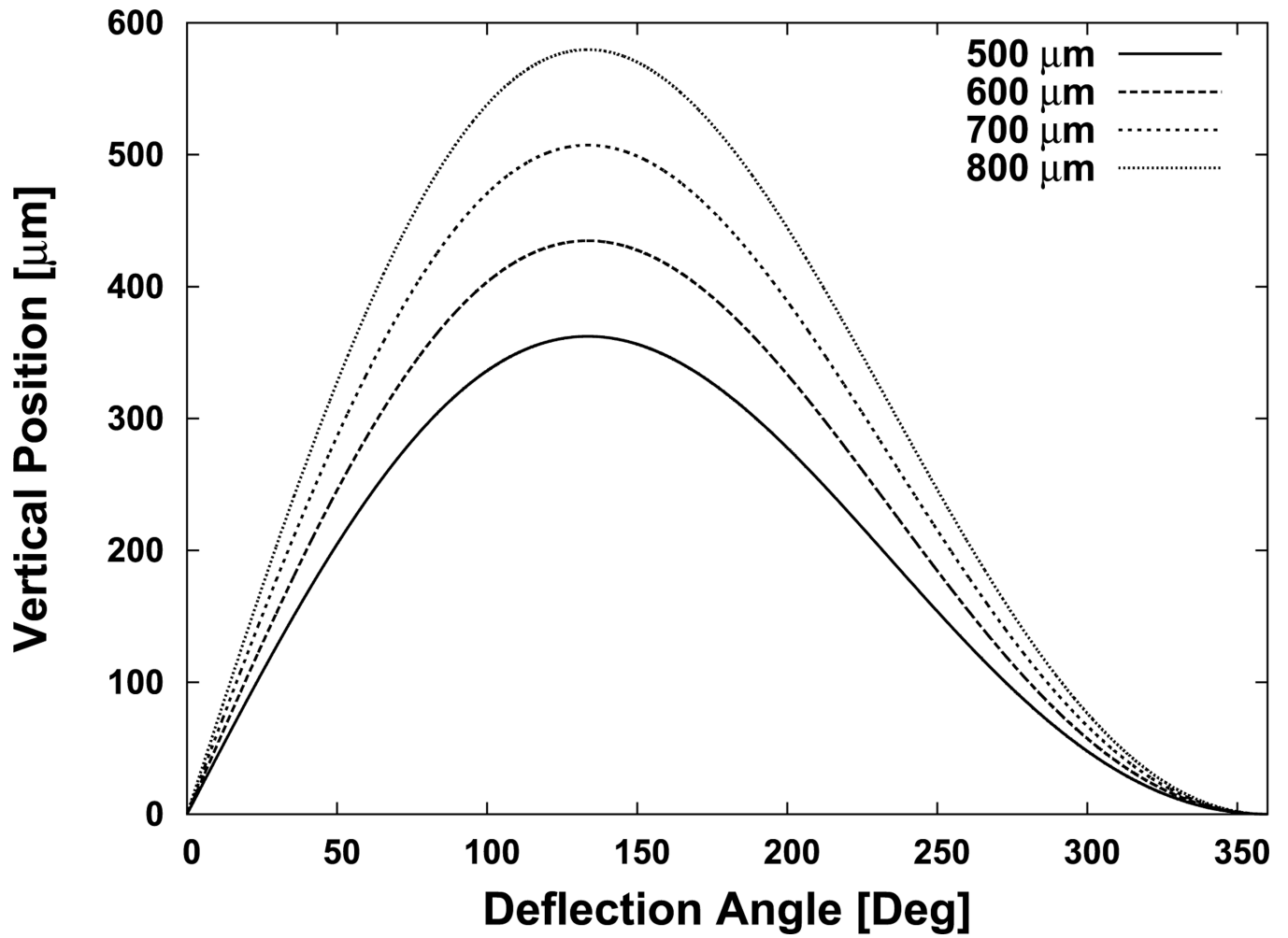
Fig. 9.
Plot of the computed z-axis deflection magnitude in relation to the deflection angle for various beam lengths.
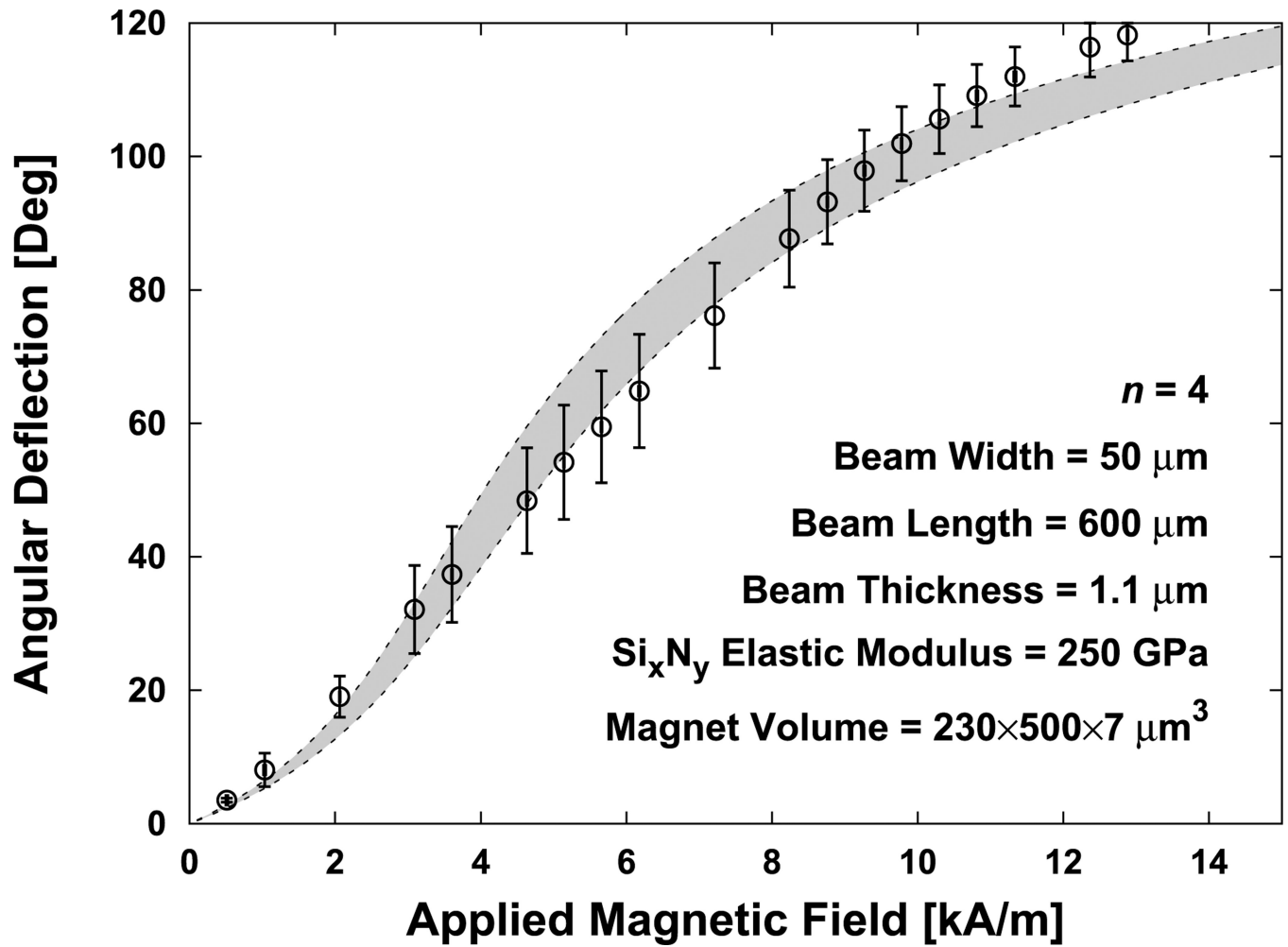
Fig. 10.
Static response of cantilever-based magnetic microactuators. The dotted line indicate theoretical static response as described by Eq. 8 using the upper ($M = 0.65$ T) and lower bounds ($M = 0.55$ T). The results are expressed as average $\pm$ s. d.
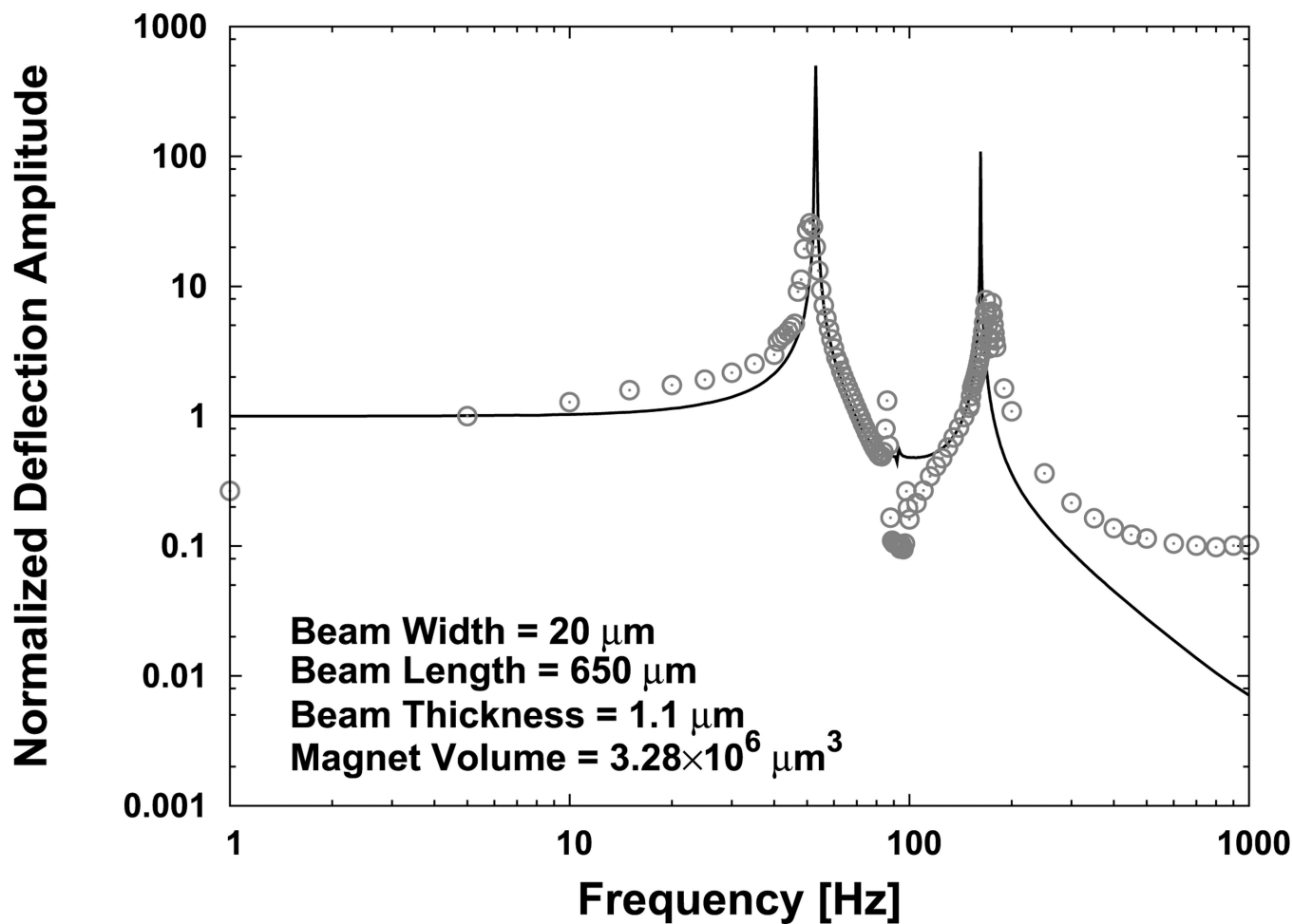
Fig. 11.
Dynamic response of a cantilever-based unobstructing magnetic microactuator. The line indicates the theoretical values obtained from COMSOL simulations. The circles indicate measured response. See Table IV.
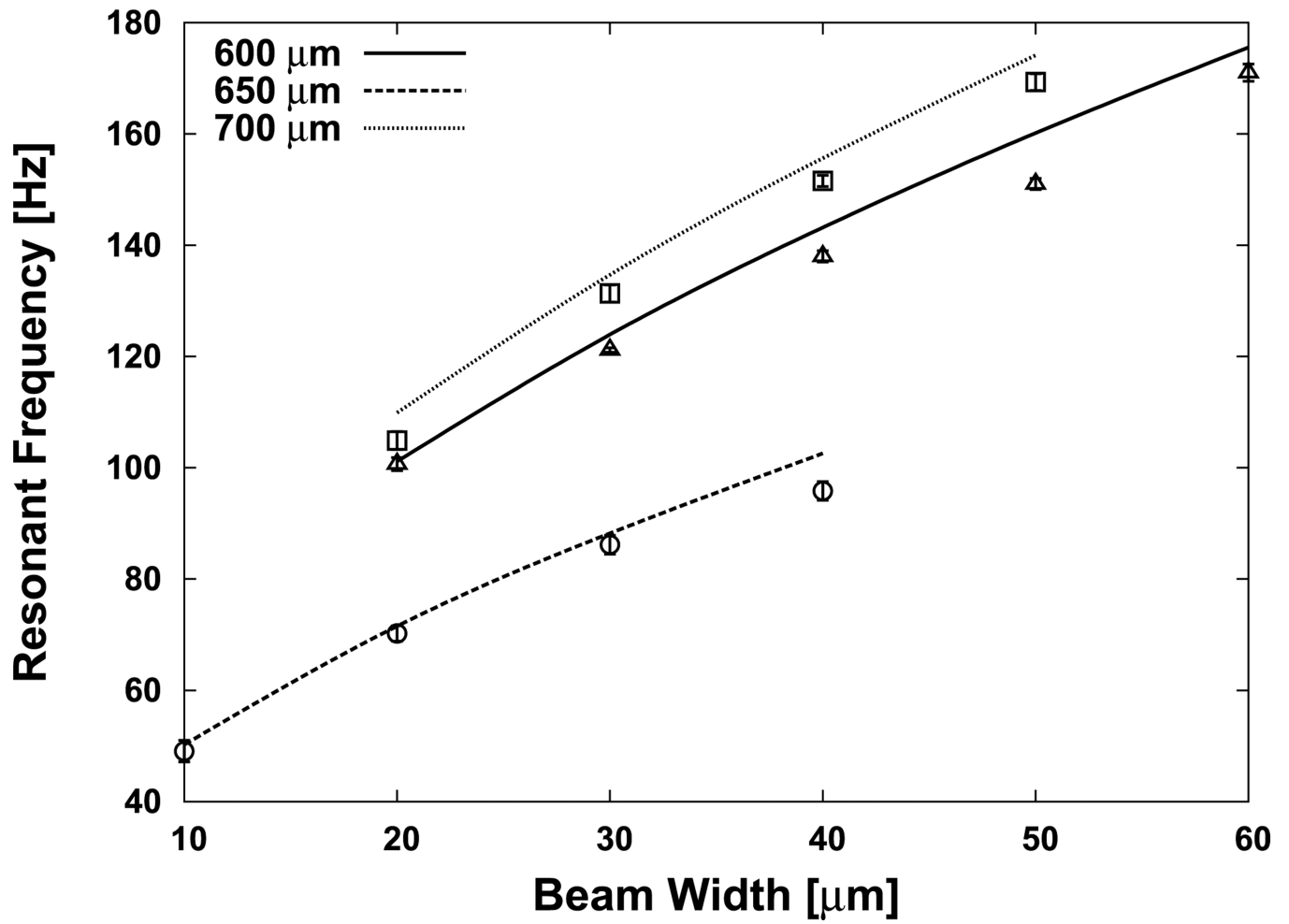
Fig. 12.
Dynamic responses of various cantilever-based magnetic microactuator designs. Each line indicates the theoretical values for the respective group of devices.

TABLE I

Parameters Used for Beam-Bending Simulations

	Beam Layer LPCVD Si_xN_y	Stressed Layer PECVD Si_xN_y
Elastic Modulus	250 GPa	110 GPa
Poisson's Ratio	0.25	0.25
Intrinsic Stress	200 MPa	−1GPa
Thickness	1 μm	100 nm

TABLE II

Percent Difference Between Measured and Theoretical Post-Release Deflection

		Beam Width [μm]					
		10	**20**	**30**	**40**	**50**	**60**
Beam Length [μm]	600	4.15	2.63	−1.59	−5.21	−4.65	−4.74
	700	−0.09	3.56	0.09	−3.5	−3.4	−2.8
	800	−2.99	2.13	−0.63	−1.89	−2.32	−0.84

TABLE III

Resonant Frequency Simulation Parameters

Beam Length	600 μm
Beam Width	20 μm
Beam Thickness	1.1 μm
Beam Elastic Modulus	250 MPa
Structural Plate Area	1.3×10^6 μm^2
Structural Plate Density	7800 kg/m
Magnet Volume	8.1×10^6 μm^3
Magnet Density	3100 kg/m

TABLE IV

Dynamic Response: Measured vs. Simulated

	Primary	Secondary	Tertiary
Measured	51 Hz	87 Hz	175 Hz
FEM	52.9 Hz	92 Hz	162 Hz
Rayleigh-Ritz	53.7 Hz	—	—